Nano Energy 69 (2020) 104398

Contents lists available at ScienceDirect

Nano Energy

journal homepage: http://www.elsevier.com/locate/nanoen

Full paper

# Comprehensively-upgraded polymer electrolytes by multifunctional aramid nanofibers for stable all-solid-state Li-ion batteries

Lehao Liu [a], Jing Lyu [b], Jinshan Mo [a], Hejin Yan [a], Lele Xu [c], Peng Peng [a], Jingru Li [a], Bing Jiang [a], Lihua Chu [a], Meicheng Li [a,*]

[a] State Key Laboratory of Alternate Electrical Power System with Renewable Energy Sources, School of Renewable Energy, North China Electric Power University, Beijing, 102206, China
[b] Suzhou Institute of Nano-tech and Nano-bionics, Chinese Academy of Sciences, Suzhou, 215123, China
[c] BOE Technology Group Co., Ltd, Beijing, 100001, China

ARTICLE INFO

*Keywords:*
Polymer electrolyte
Aramid nanofiber
Ion conductance
Mechanical property
Lithium ion battery

ABSTRACT

Satisfactory ionic conductivity and mechanical stability are the prerequisites for the applications of solid polymer electrolytes in Li-ion batteries. Herein, by using aramid nanofibers (ANFs) as multifunctional nano-additives, comprehensively-upgraded polyethylene oxide (PEO)-LiTFSI electrolytes with 3D ANF network frames are achieved through the hydrogen-bond interactions between the 1D ANFs. The hydrogen-bond interactions between the ANFs and the PEO chains and $TFSI^-$ anions can greatly prevent the ANF agglomeration, suppress the PEO crystallization, facilitate the LiTFSI dissociation, and prolong the ion transport paths at the 3D ANF framework/PEO-LiTFSI interfaces. Thus, the ANF-modified electrolytes show superior room-temperature conductivity of $8.8 \times 10^{-5}$ S $cm^{-1}$. The ANF-containing composite electrolytes also display greatly-enhanced mechanical strength, thermostability, electrochemical stability and interfacial resistance against Li dendrites, attributed to the 3D ANF framework. In consequence, the composite electrolyte-based $LiFePO_4$/Li cells exhibit better rate performance and cycling stability (e.g., 135 mAh $g^{-1}$ after 100 cycles at 0.4 C). This work offers a novel and effective strategy to comprehensively upgrade polymer electrolytes by employing organic nanofillers in the composite electrolyte design and revealing the ion transport mechanism for promising all-solid-state Li-ion battery applications.

## 1. Introduction

Lithium-ion batteries (LIBs) are widely applied in many areas such as portable devices and electric vehicles [1]. Nevertheless, the utilization of organic liquid electrolytes elicits severe safety issues resulted from the leakage, volatility, flammability, dendrite formation, and side reactions [2,3]. The replacement of these liquid electrolytes with solid-state electrolytes (SSEs) cannot only circumvent the safety problems, but also achieve high-energy-density solid-state batteries by using high-capacity cathodes and Li metal anodes [4–6]. Additionally, the battery fabrication processes would be simplified by removing polymer separators [7]. Compared to ceramic-type SSEs, solid polymer electrolytes (SPEs) comprised of polymer matrices and Li salts have higher flexibility, easier film-forming ability and lower interface resistance with the electrodes, and are suitable for solid-state LIBs [3,8–12]. Especially, polyethylene oxide (PEO) with the soft chains is regarded as an excellent electrolyte matrix, owing to its strong capability to dissolve Li salts and low cost [13–15]. However, the applications of the SPEs are restricted by the unsatisfactory ionic conductivity and mechanical properties that can easily cause the penetration by Li dendrites [10,16–19].

Designing composite polymer electrolytes (CPEs) by dispersing inorganic particles such as inert $TiO_2$ and active $Li_7La_3Zr_2O_{12}$ (LLZO) in the polymer matrices offers an important way to improve the properties of the SPEs [20–26]. The addition of the inorganic nanoparticles can improve the ionic conductivity of the SPEs, due to their high surface area and Lewis acid-base interaction with the anions of the electrolyte ion species, which could inhibit the polymer crystallization and facilitate the Li salt dissociation [20,27,28]. Specifically, the $Li^+$ ion conduction mostly occurs at the filler/polymer-Li salt interfaces [29–34], and controlling the filler size and dispersity is extremely important because it is related to the effective interaction areas between the fillers and the

* Corresponding author.
*E-mail address:* mcli@ncepu.edu.cn (M. Li).

https://doi.org/10.1016/j.nanoen.2019.104398
Received 18 October 2019; Received in revised form 24 November 2019; Accepted 8 December 2019
Available online 12 December 2019

polymer/Li salt matrices [24,35–38]. The further utilization of one-dimensional (1D)/2D inorganic nanofillers such as LLZO nanowire and graphene oxide can prolong the $Li^+$ ion transport pathway for higher ionic conductivity [14,27,31,32,39]. Unfortunately, the strong van der Waals forces between the large-surface-area nanofillers, poor interactions between the inorganic nanofillers and the electrolyte matrices, and the resulted poor nanofiller dispersity, high polymer crystallization and low Li salt dissociation, severely affect the electrical properties of the CPEs [40–43]. The mechanical strength and thermostability cannot be also greatly enhanced, due to the failure to form interconnected nanofiller reinforcements [19,44]. Filling polymer electrolytes in 3D porous ceramic electrolyte substrates cannot only avoid the nanofiller dispersity issue, but also enhance the ionic conductivity and mechanical stability by forming 3D continuous filler framework [5,45–49]; however, the applications of these CPEs in solid-state LIBs are severely limited by the high stiffness and brittleness of the ceramic scaffolds, and the low-efficiency fabrication processes [13,30,43].

All these fruitful researches shed lights on improving the SPE properties by applying new inorganic filling materials, designing electrolyte structures and exploring the mechanisms. Nevertheless, there are few reports on the utilization of organic nanofillers, though the possible improvement on the nanofiller compatibility/dispersity with/in the electrolyte matrices with the help of their functional groups and the strong interactions with the polymer matrices. Previous studies have confirmed that the organic molecules or polymer additives [50–52] show good compatibility with the electrolyte matrices (e.g. PEO) and can improve the ionic conductivity of the PEO-based SPEs. Besides, a few researchers have reported high-conductivity inorganic active nanofiller-modified CPEs but not yet given the solid-state battery performance at low operation temperatures [20,27,33,53–56], which is vital to their practical applications. With these considerations, we are wondering if there is a multifunctional organic nanofiller that combines the advantages of the organic additives (functional groups for compatibility/dispersity with/in the electrolyte matrices), inorganic nanofillers (1D/2D morphologies for long ion transport paths), and 3D porous ceramic substrates (3D nanofiller frame for continuous ion migration routes and high mechanical stability) to greatly improve the overall electrolyte properties for their practical battery applications.

Aramid fibers constituted with polyparaphenylene terephthalamide (PPTA) molecules have combined characteristics such as abundant amide groups, large aspect ratio, high mechanical tensile strength (up to 3.8 GPa), high thermo-decomposition temperature (500 °C), light weight, high chemical inertness and low electrical conductivity, and are widely used to prepare body armors and other high-strength products [57–59]. Nevertheless, their applications in nanocomposites are hindered by the macroscale of the commercial aramid fibers. Since the discovery of stable aramid nanofiber (ANF) dispersion by Kotov group, there are a lot of interesting works on the 1D ANF-reinforced nanocomposites [57–62]. We have employed the ultralong ANFs to fabricate flexible ANF films [57] and ANF/Au (Ag) [58,59] nanocomposite conductors with 3D ANF networks through the hydrogen-bond interactions between the amide groups in ANFs. ANF/polypropylene and ANF/PEO composite membranes were also prepared as high-performance separators in the organic liquid electrolyte-based LIBs, owing to the effective inhibition of the Li dendrite growth by the high-strength ANFs [60,61]. Moreover, the polar carbonyl groups in the polyamides can also greatly increase the electrolyte wettability of the separators for higher ionic conductivity [63,64]. Poly(m-phenylene isophthalamide) (PMIA), another aromatic polyamide with meta-type benzene-amide linkages in its skeletal chain, has also been fabricated as separators with great enhancements in thermostability and electrochemical stability [63]. Thus, ANF may act as a proper multifunctional nanofiller to comprehensively upgrade the SPE properties such as ion conductance, mechanical strength and thermostability.

Herein, we aim to fabricate comprehensively-improved PEO-LiTFSI electrolytes by employing the multifunctional ANFs as nanofillers based on the following considerations: (1) the hydrogen-bond interactions between the amide groups of the ANFs and the PEO chains and $TFSI^-$ anions would effectively prevent the ANF agglomeration in the electrolyte matrices, suppress the PEO crystallization, promote the LiTFSI dissociation, and thus elevate the ionic conductivity of the CPEs (Fig. 1A); (2) the ultralong 1D ANFs with large aspect ratio would lengthen the $Li^+$ ion transport paths at the ANF/PEO-LiTFSI interfaces (Fig. 1B); (3) the hydrogen-bond interactions between the ANFs can induce the formation of 3D ANF networks in the CPEs, and thereby lead to the simultaneous enhancement of the mechanical/thermal stabilities and the ionic conductivity by forming 3D continuous ion conduction routes at the ANF framework/PEO-LiTFSI interfaces (Fig. 1B). As is verified by various measurements, the ANF-modified electrolytes exhibit greatly-improved ionic conductivity, mechanical properties, thermostability, electrochemical stability, and resistance against Li dendrites. When paired with conventional $LiFePO_4$ cathodes and Li anodes, the ANF/PEO-LiTFSI CPE-based solid-state cells display superior rate performance and cycling stability. Hence, this CPE design criteria with multifunctional organic nanofillers and the ion transport mechanism open a new way to achieve comprehensively-upgraded electrolytes for high-energy and safe LIBs.

## 2. Results and discussion

### 2.1. Microstructure and morphology

To prepare the ANF/PEO-LiTFSI CPE films by the traditional solution casting method (Fig. S1), we first prepared ANF-containing dimethylformamide (DMF)/dimethylsulfoxide (DMSO) solutions with high ANF dispersity demonstrated by the optical photographs (Fig. 1C). After the dissolution of PEO and LiTFSI and the following drying process, high-flexibility and semi-transparent ANF/PEO-LiTFSI CPE films can be easily fabricated (Fig. 1D). The CPE films with 0, 1, 3, 5, 10 and 20 wt% ANFs were denoted as ANF0, ANF1, ANF3, ANF5, ANF10 and ANF20, respectively. It should be also noted that a few pores and cracks formed during the drying process when the ANF content exceeded 10 wt%, because of the increasing viscosity of the ANF solution and fast solvent evaporation in vacuum. With the help of SEM technology, we can see that the electrolytes without and with low-content ANFs show the similar surficial and cross-sectional morphology, and many wrinkles formed at the electrolyte surfaces (Fig. 1E–H and Fig. S2A-B). However, a few pores generated in the 10 wt% ANF-containing CPEs (Fig. S2C–D). The energy dispersive X-ray spectroscopy (EDS) mapping images furtherly verified the effective incorporation of the ANF nanofillers in the PEO/LiTFSI matrices by the solution casting method (Fig. S3).

In the high-resolution TEM images, the ultralong 1D ANFs with an average diameter of 9.4 nm formed a network structure due to the strong hydrogen-bond interactions between their amide groups (Fig. 1I), consistent with our previous works [57–59]. Compared to the pristine PEO-LiTFSI electrolyte (Fig. 1J), the ANFs still remained the high dispersity and network constitution in the ANF-containing electrolyte (Fig. 1K). The average diameter of the ANFs in the CPE was calculated to be 8.5 nm, attributed to the strong interactions between the ANFs and the PEO/LiTFSI matrices and their high compatibility. Different from the inorganic nanofillers with aggregation behaviors and poor particle-to-particle connections, the high ANF dispersity and the continuous networks in the CPEs would be beneficial to the electrolyte properties such as ionic conductivity and mechanical strength.

### 2.2. Ionic conductivity

The ionic conductivity ($\sigma$) can be described with the classic equation (1): $\sigma = \Sigma C_i Q_i \mu_i$, where $Q_i$, $C_i$ and $\mu_i$ represent the charge, concentration and mobility of the charge carriers, respectively [65,66]. In typical polymer electrolyte systems, the dominated cation motions occur in the

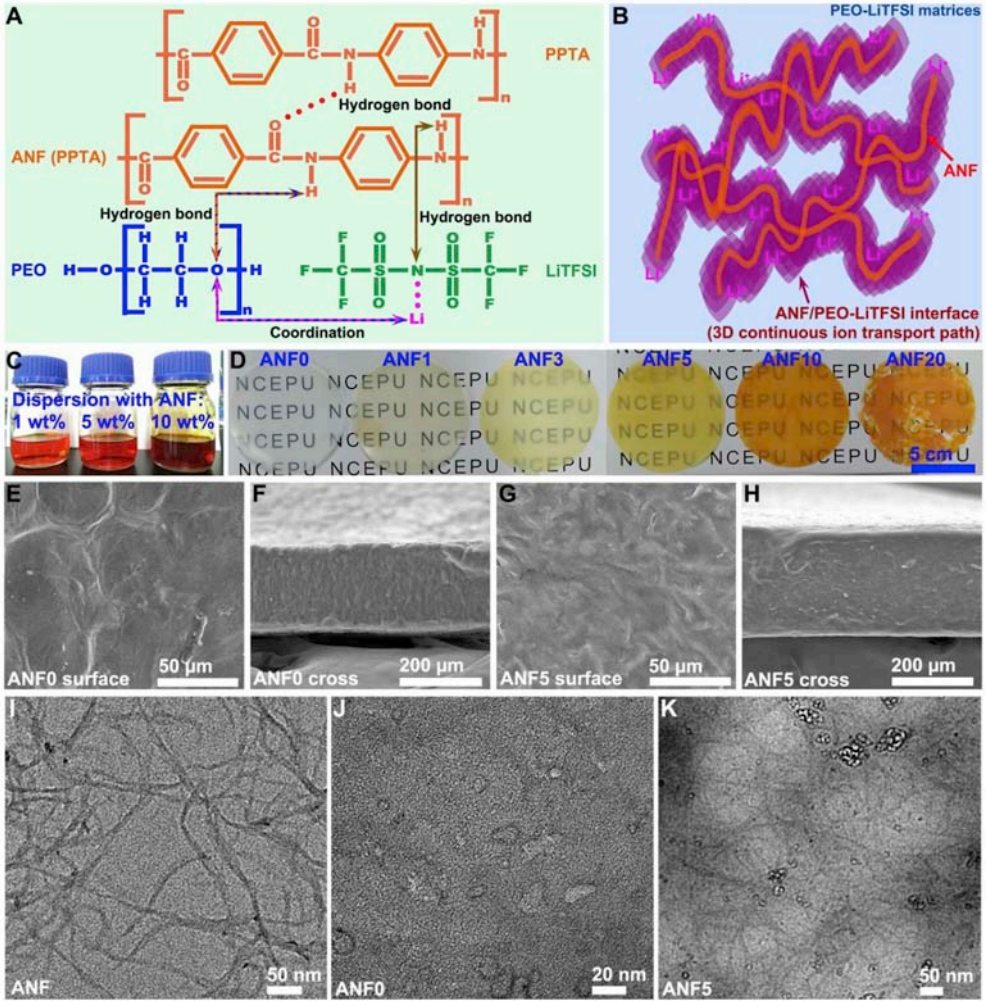


**Fig. 1.** Schematic illustration of (A) the interactions between ANFs and PEO chains and LiTFSI, and (B) the ion transport paths in ANF/PEO-LiTFSI CPEs. Optical images of (C) ANF/DMF/DMSO solutions and (D) CPE films, and (E, G) surficial and (F, H) cross-sectional SEM images of the CPEs with (E–F) 0 and (G–H) 5 wt% ANFs, respectively. TEM images of (I) ANFs, and (J) 0 and (K) 5 wt% ANF-containing CPEs (diluted ANF/PEO/LiTFSI solutions with DMF for TEM characterization), respectively.

amorphous polymer regions through the local segmental chain motion, which is considered as the driving force for the ion transport and affects the ion mobility [32,65–68]. The interactions between the components in the polymer electrolytes also have an important influence on the free ion concentration. As we know that the elements of Li, H, S, N, Cl, O and F have the electronegativity values of 0.98, 2.18, 2.58, 3.04, 3.16, 3.44 and 3.98, respectively. There is an ion-dipole or coordination interaction between the –O– groups in PEO and the $Li^+$ cations in Li salts [65]. The hydrogen-bond interactions between the –NH groups in polyamides and the –O– groups in PEO can afford their layer-by-layer assembly for composite membranes [69,70]. Moreover, it has proven the existence of strong hydrogen-bond interactions between the –NH groups in PMIA and the $Cl^-$ anions in LiCl [71]. A few researchers furtherly find that urea calix[2]-p-benzo[4]pyrroles [72] and calis[4]arene [73,74] can capture the anions (e.g., $ClO_4^-$) of Li salts by hydrogen-bond interactions through their –NH groups, and thus release more free $Li^+$ ions in the electrolytes. Therefore, the ANFs (exactly the –NH groups in PPTA) should have hydrogen-bond interactions with both the –O– groups in PEO and the $TFSI^-$ anions in LiTFSI in theory (Fig. 1A–B), and would have great impact on the polymer electrolytes (e.g., $C_{Li}$ or $\mu_{Li}$ of the $Li^+$ ion).

Fourier transform infrared (FT-IR) measurements were performed to investigate the interactions between the ANF nanofillers and PEO/LiTFSI (Fig. 2A–B). A few typical absorbance peaks at 850, 1466 and 2890 $cm^{-1}$ related to the $CH_2$ and C–H stretching and bending appeared in the PEO-LiTFSI electrolyte film, and other important peaks at 788, 952, 1055, 1104, 1188, 1230 and 1345 $cm^{-1}$ were ascribed to the stretching and bending vibrations of C–O and C–O–C groups of the PEO matrices [28,75]. The PEO-LiTFSI electrolyte also showed obvious peaks at 572, 740, 760 and 1285 $cm^{-1}$, which were attributed to the stretching vibration of $CF_3$ and C–F groups in LiTFSI [76,77]. Other characteristic peaks at 653, 1140 and 1634 $cm^{-1}$ also appeared in the PEO-LiTFSI electrolyte, and were related to the S–O stretching, C–$SO_2$–N stretching and LiTFSI aggregation, respectively [76,77]. The stretching and bending of the N–H bands in the ANF film were located at 724, 1512 and 3320 $cm^{-1}$, and the peaks at 1647 and 1544 $cm^{-1}$ corresponded to the C═O and C–N stretching also appeared in the ANF film, respectively.

We can easily observe the changes of the FT-IR spectra to disclose the effects of the ANF nanofillers on the PEO-LiTFSI electrolyte. The obvious peak shifting of the N–H bands from 724 $cm^{-1}$ in the ANF film to 708 $cm^{-1}$ in the ANF-containing electrolyte, and other peak position and shape changes of the C═O and C–N bands of the ANFs together indicated the strong interactions between the ANFs and the PEO/LiTFSI matrices. Compared to the pristine PEO-LiTFSI electrolyte, the C–O–C stretching-resulted peak positions shifted from 952 to 960 $cm^{-1}$ and from 1230 to 1239 $cm^{-1}$ (in the 5 wt% ANF/PEO-LiTFSI electrolyte), and the shapes of the absorbance peaks at 950–1150 $cm^{-1}$ also changed significantly. These obvious changes should be attributed to the hydrogen-bond interactions between the N–H groups of the ANFs and the C–O–C groups of the PEO matrices, which effectively prohibited the ANF aggregation in the CPEs (Fig. 1K), and meanwhile perturbed the ordering of the PEO chains and thus suppressed the PEO crystallization, which was proved by the XRD tests (Fig. 2E). Specifically, the intensity of the typical peaks at around 19.5 and 23.6° related to the PEO

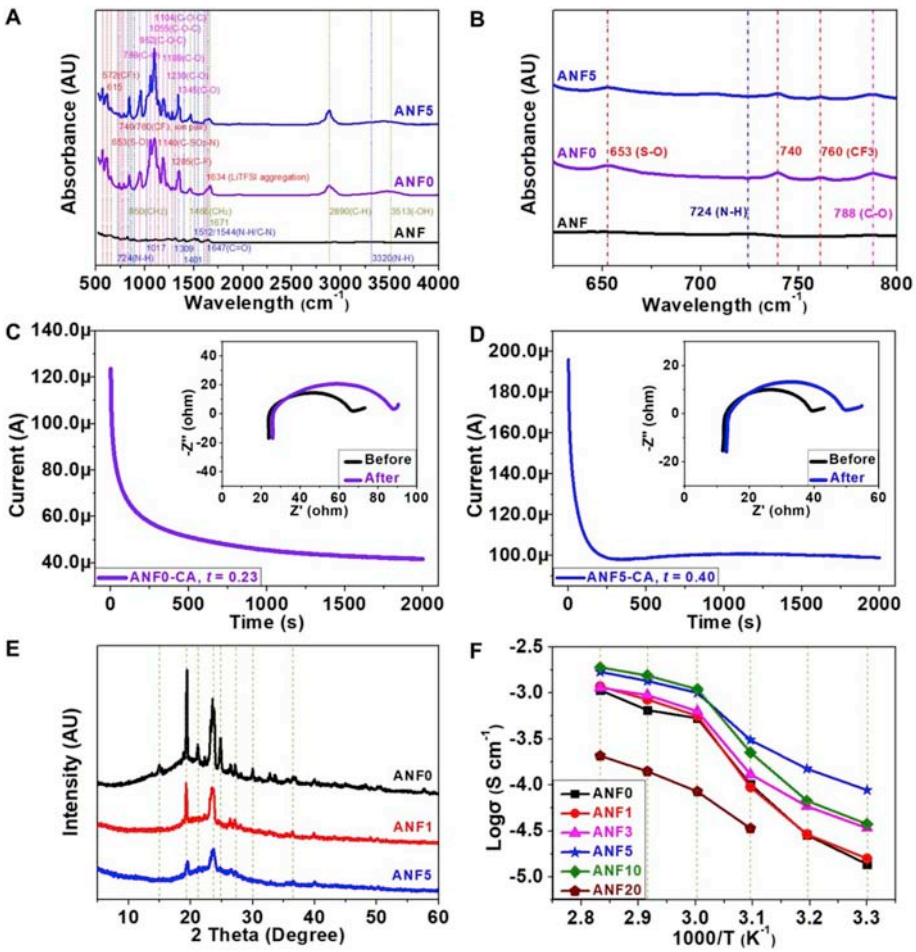


**Fig. 2.** (A–B) FT-IR spectra of the ANF and electrolyte films. The chronoamperometry (CA) curves of Li/electrolyte/Li cells under a potential step of 0.01 V at 80 °C for the (C) ANF-free, and (D) 5 wt% ANF-containing electrolytes, respectively. The insets showed the corresponding EIS spectra before and after the polarization tests. (E) Typical XRD patterns, and (F) ionic conductivity of the electrolyte films.

crystallinity degree became weaker in the ANF-containing electrolytes, manifesting the effective inhibition of the PEO crystallization by the ANF nanofillers. The suppression of the PEO crystallization would accelerate the segmental chain movements in the amorphous areas, and thereby elevate the $Li^+$ cation mobility ($\mu_{Li}$) by hopping between/along the PEO chains [65].

Moreover, the intensity of the peaks at around 740 and 760 $cm^{-1}$ corresponding to the ion pairs in LiTFSI decreased greatly with the addition of the ANFs, indicating that less triflate-containing anions were in pairs in the ANF-filled electrolytes [77]. The peak intensity at around 1634 $cm^{-1}$ representing the LiTFSI aggregation [76] also decreased, furtherly suggesting the strong hydrogen-bond interactions between the N–H groups of the ANFs and $TFSI^-$, and the effective promotion of the LiTFSI dissociation. Specifically, the hydrogen-bond interactions between the –NH groups in PMIA and the $TFSI^-$ anions (mainly the F atoms, due to the high F electronegativity and the F-related peak change) resulted in the effective dissociation and dissolution of LiTFSI, based on the FTIR analyses, the elemental electronegativity values and the reports from other researchers [71–74]. To accurately verify the impact of the ANF additive on the LiTFSI dissociation, the $Li^+$ ion transference numbers ($t_{Li}^+$) of the electrolytes were calculated with the combination of chronoamperometry (CA) and electrochemical impedance spectroscopy (EIS) tests. $t_{Li}^+$ of the 5 wt% ANF-containing electrolyte was 0.40 (Fig. 2D and Table S1), which was nearly two times that of the pristine electrolyte (0.23, Fig. 2C) in accordance with the previous reports (0.2–0.3) [35,38,78–80], once again proving the effective facilitation of the LiTFSI dissociation by the ANF nanofillers and the anion capture capability of the ANFs. The release of $Li^+$ cations from LiTFSI would increase the $Li^+$ cation concentration ($C_{Li}$) to improve the $Li^+$ ion conduction, while the immobilization of the $TFSI^-$ anions on the ANF fillers could be beneficial to reduce the electrode polarization and prevent the Li dendrite growth [81,82].

According to the ion conductance equation (1): $\sigma = \Sigma C_i Q_i \mu_i$, either increase of the $C_i$ or $\mu_i$ can contribute to the enhancement in the electrolyte conductivity. In the ANF/PEO-LiTFSI electrolyte system, because of the positive synergistic effects of the ANF nanofillers on PEO and LiTFSI (i.e., the increase in $\mu_{Li}$ and $C_{Li}$), the CPE with 5 wt% ANFs exhibited much higher ionic conductivity of $8.8 \times 10^{-5}$ and $1.0 \times 10^{-3}$ S $cm^{-1}$ than the pristine PEO-LiTFSI electrolyte ($1.3 \times 10^{-5}$ and $5.3 \times 10^{-4}$ S $cm^{-1}$) at 30 and 60 °C, respectively (Fig. 2F). The excellent $Li^+$ ion conduction property of the 5 wt% ANF-containing CPEs was even comparable to the active nanofiller- or 3D inorganic ceramic electrolyte scaffold-based CPEs (Table S2). However, the addition of high-content ANFs (10 and 20 wt%) resulted in the decreasing ionic conductivity, ascribed to the formed pores/cracks in the CPE films to destroy the ion migration routes or the blocking of the ion transfer by the non-ion-conducting ANF nanofillers.

The relationship between the ionic conductivity and the temperature follows the classic Arrhenius relationship equation (2): $\sigma = A\exp(-E_a/RT)$, where $A$, $E_a$, $R$, *and* $T$ represent the pre-exponential factor, activation energy, gas constant (8.314 J $mol^{-1}$ $k^{-1}$), and absolute temperature, respectively [27]. The activation energies of the CPEs with various ANF contents were given in Table S3. In the low temperature range of 30–60 °C, the 5 wt% ANF/PEO-LiTFSI CPE had much lower activation

energy of 66.9 kJ $mol^{-1}$ than the PEO-LiTFSI electrolyte (102.1 kJ $mol^{-1}$), which was consistent with the Arrhenius plots where the 5 wt% ANF/PEO-LiTFSI CPE showed the smaller slop. The low activation energy indicated that there was a low-energy-barrier ion conduction pathway in the ANF-modified CPEs [28], i.e., a diverse conduction mechanism rather than the ion random walking through the amorphous polymer matrices for the CPEs [27].

It is widely accepted that there are three phases in the nanofiller-modified SPEs, i.e., the nanofiller, filler/polymer-Li salt interface (or on the nanofiller surface) and polymer-Li salt regions, and $Li^+$ ions transport in these phases at different speed [32,83–86]. As for the active nanofiller-containing CPEs, $Li^+$ ions were usually thought to transport mainly at the interfaces or inside the particles; however, recent solid-state nuclear magnetic resonance (ssNMR) researches show that $Li^+$ ions mostly transfer on the surfaces of the active nanofillers such as $Li_7La_3Zr_2O_{12}$ [33], $Li_{3/8}Sr_{7/16}Ta_{3/4}Zr_{1/4}O_3$ [29] and $Li_{10}GeP_2S_{12}$ [34]. Numerical analyses (e.g., Comsol Multiphysics) furtherly reveal that the interfacial conductivities of the $Li_{0.33}La_{0.557}TiO_3$ nanowire ($1.3 \times 10^{-2}$ S $cm^{-1}$ at 30 °C) [32] and $Li_{1.3}Al_{0.3}Ti_{1.7}(PO_4)_3$ nanoparticle ($2.0 \times 10^{-4}$ S $cm^{-1}$ at 20 °C) [83] modified CPEs were much higher than the active nanofillers and comparable to the ion conductivity of the organic liquid electrolytes. As for the inert nanofiller-based CPEs, $Li^+$ ion conduction mainly occurs at the interface regions due to the non/low-conductivity of the inert nanofillers [31,80,84,87].

In our ANF/PEO-LiTFSI electrolyte system, there are also three different ion conduction regions, i.e., PEO-LiTFSI, ANF-LiTFSI and ANF/PEO-LiTFSI interface phases. The existence of the ANF/PEO-LiTFSI interfacial phase was attributed to the hydrogen-bond interactions between the ANFs and PEO and LiTFSI, confirmed by the characterizations such as TEM and FTIR. In accordance with other reports on the rigid amide-benzene backbone-based polymer electrolytes [81,88,89], the PPTA-LiTFSI electrolyte with ~26 wt% LiTFSI showed a room-temperature ionic conductivity of $9.2 \times 10^{-8}$ S $cm^{-1}$ (Fig. S4), which was around two and three orders of magnitude lower than the PEO-LiTFSI electrolyte ($1.3 \times 10^{-5}$ S $cm^{-1}$) and 5 wt% ANF/PEO-LiTFSI CPE ($8.8 \times 10^{-5}$ S $cm^{-1}$), respectively. The PPTA-LiTFSI electrolyte also exhibited much higher activation energy of 199.7 kJ $mol^{-1}$ than the PEO-based electrolytes at 30–60 °C (Table S3). Both these results proved that the aramid nanofibers were inert or low-conducting nanofillers, and also suggested that the great enhancement on the CPE conductivity was ascribed to the low-barrier ion conduction pathways at the ANF/PEO-LiTFSI interfaces (or on the ANF surfaces) rather than in the ANF nanofillers or the PEO-LiTFSI matrices.

The density function theory (DFT)-based first-principles computation was further employed to disclose the $Li^+$ ion transport mechanism. The optimized structure of the $Li^+$ ions coordinated with the low-molecular species of PPTA and PEO, and the corresponding binding energy ($E_b$) of the $Li^+$ ion interactions with the low-molecular PPTA and PEO were given in Figs. S5A–E. The Li···O–C binding energy (78 kJ $mol^{-1}$ in the low-molecular PEO-Li system) was comparable to the Li···N–H binding energy (79 and 58 kJ $mol^{-1}$) but much lower than the Li···O═C binding energy (144 and 180 kJ $mol^{-1}$ in the low-molecular PPTA-Li system), indicating that PPTA had much higher binding energy with $Li^+$ ions than PEO. The stronger coordination strength between $Li^+$ ions and PPTA can facilitate the LiTFSI dissociation to increase the ion concentration, while the hydrogen-bond interaction between $TFSI^-$ and PPTA can also facilitate the LiTFSI dissociation (Fig. 2A–B); however, the PPTA-LiTFSI electrolyte had the lowest ionic conductivity (Fig. S4), due to the stronger coordination strength between the ions and PPTA and the higher steric hindrance of the rigid PPTA chains. In the ANF/PEO-LiTFSI electrolyte system, the PPTA chains in the ANF nanofillers strongly linked with each other through the hydrogen-bond interactions without effective contact with LiTFSI, and thus the $Li^+$ ion conduction can only occur on the nanofiller surfaces. Solid-state NMR showed that LiTFSI in the pristine PEO-LiTFSI electrolyte had a $^7Li$ NMR peak at 0.36 ppm, but the LiTFSI resonance in the ANF/PEO-LiTFSI electrolyte became broadening (Fig. S5F). This indicated that the ANF nanofillers can increase the disorder of the $Li^+$ ion local environment by inhibiting the PEO crystallization, and also suggested an ion-conducting interface on the nanofiller surface with PEO. On the contrary, the lower coordination strength between $Li^+$ ions and PEO was detrimental to the LiTFSI dissociation for free ions, but can promote the repeated bonding/releasing of the $Li^+$ ions with/from the soft PEO chains, resulting in the higher ionic conductivity of the PEO-LiTFSI electrolyte than that of the PPTA/LiTFSI electrolyte. Owing to the high ion concentration and the fast PEO chain motion at the ANF nanofiller/PEO interfaces (or on the ANF surfaces, Fig. S5G), the ANF/PEO-LiTFSI CPEs exhibited the greatly-improved ionic conductivities.

Our experimental characterizations combined with the famous Lewis acid-base theory can also verify the main ion transport pathway at the ANF/PEO-LiTFSI interfacial regions. On one hand, the ANF nanofillers acted as cross-linking centers for PEO chains by the hydrogen-bond interactions (Fig. 2A) and inhibited the PEO chains to reorganize themselves (Fig. 2E), thus promoting the preferred $Li^+$ ion conduction on the amorphous nanofiller surfaces due to the fast PEO chain motions [80,90]. The hydrogen-bonding between the ANF nanofillers and PEO can also weaken the coordination strength between the $Li^+$ ions and the –O– groups in PEO and therefore increase the free $Li^+$ ion concentration on the nanofiller surfaces [65,91]. On the other hand, the hydrogen-bonding between the nanofillers and the Li salts can capture the anions and emancipate more free $Li^+$ cations on the ANF nanofiller surfaces (Fig. 2A–B and D), resulting in a fast pathway for $Li^+$ ion diffusion at the interfacial region along the ANF nanofillers [27,92]. Besides, the 3D ANF networks formed by the ultralong nanofillers through hydrogen-boning can offer 3D continuous $Li^+$ ion-conducting channels on the nanofiller surfaces (Fig. 1K), in sharp contrast to the incontinuous transfer channels by most of the isolated inorganic nanofillers in polymer matrices [27]. Based on the abovementioned analyses, it was reasonable that $Li^+$ ions mainly transported at the ANF/PEO-LiTFSI interface phase rather than in the inert ANF or PEO-LiTFSI regions in the low temperatures of ≤60 °C (Fig. 1B and Fig. S5G). However, in the high temperature range of 60–80 °C, all the PEO-based electrolytes exhibited much lower yet similar activation energy of ~30 kJ $mol^{-1}$, owing to the increased mobility of the ions and the polymer chains caused by the temperature increase [67,68], and the PEO-LiTFSI phase played more and more important role in the ion transport.

### 2.3. Electrochemical, mechanical and thermal properties

In addition to the $Li^+$ ion conductivity, other properties including the electrochemical stability, mechanical strength and thermal stability also affect the applications of the SPE-based LIBs. The electrochemical stability of the CPEs were measured by linear sweep voltammetry (LSV) in the stainless steel/SPE/Li coin cell configuration, and the high-content ANFs (≥5 wt%) in the electrolytes can broaden the electrochemical window (Fig. 3A). The mechanical tensile measurements showed that the 5 wt% ANF-containing electrolyte film displayed higher ultimate tensile stress of 2.5 MPa and lower tensile strain of 338.0% than the pristine electrolyte film (0.4 MPa and 1572.3%, Fig. 3B), due to the 3D ANF network frames in the composite films (Fig. 1K). The 5 wt% ANF/PEO-LiTFSI CPE membrane also exhibited a Young's modulus of 18.5 MPa, which was 20.6 times higher than the pristine one (0.9 MPa).

Furthermore, the 5 wt% ANF/PEO-LiTFSI electrolyte showed higher thermal decomposition temperature of around 410 °C than the pristine electrolyte (367 °C, Fig. 3C), also attributed to the high-stability ANF network structure. The superior thermostability of the ANF-filled CPE films was also verified by observing the shape and color changes of the circular films at 160 °C in air (Fig. 3D). The pristine sample melted after 0.5 h, but the ANF-containing CPE films with moderate content (≥3 wt %) still kept the original shape and color even after 10 h, indicating the enhancement of the thermal stability by the ANF nanofillers. The high

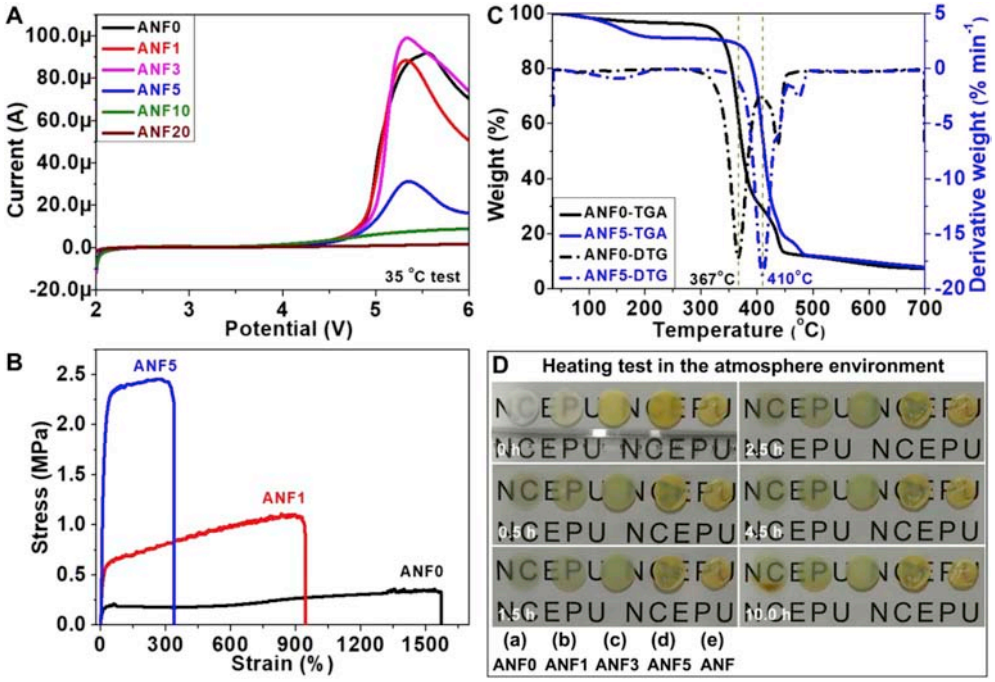


**Fig. 3.** (A) Linear sweep voltammetry (LSV) profiles, (B) mechanical tensile stress-strain curves, (C) TGA curves, and (D) optical photos at 160 °C for various hours in an oven of the different electrolyte films.

mechanical strength and thermostability of the CPEs would effectively delay the nucleation of Li dendrites, and prevent the crack generation in the electrolytes when the Li dendrites penetrate into the electrolytes [35].

### 2.4. Resistance against Li dendrites

The mechanical stability of the electrolyte films against Li dendrites was studied by using symmetric Li/SPE/Li cells, which is also vital to the applications of the SPEs in the solid-state LIBs. $Li^+$ ions were plating/stripping on the Li metal electrodes during the periodic charge-discharge processes. When tested at a high temperature of 60 °C, the cell with the pristine PEO-LiTFSI electrolyte had an initial over-potential of 0.0260 V at 0.05 mA $cm^{-2}$, and the over-potential increased with the increase of current density and reached 0.9003 V at 0.50 mA $cm^{-2}$ (Fig. 4A). The potential was around 0.0388 V when the current density returned to 0.05 mA $cm^{-2}$ after 200 h. In sharp contrast, the ANF-containing cells showed lower over-potentials (Fig. 4B and S6A-B), indicating the lower interfacial resistance between the ANF-filled CPE films and Li metal electrodes. Amongst the electrolyte films, the 5 wt% ANF/PEO-LiTFSI film-based cell showed the lowest over-potentials.

When tested at a lower temperature of 30 °C with a charge-discharge cycle of 10 min, the ANF-free cell displayed a high over-potential of 2.1587 V at 0.10 mA $cm^{-2}$, and the over-potential decreased to 0.6231 V after 500 h (Fig. 4C), because of the improved interface contact between the electrolyte films and Li metal electrodes [5]. In comparison, the ANF-containing cells showed lower over-potentials (Fig. 4D and S6C-D). When increasing the charge-discharge time to 60 min per cycle, the cell with the pristine electrolyte showed high overpotentials at 30 °C and 0.10 mA $cm^{-2}$, and suddenly the potential decreased from around 1.25 to 0 V after 5.5 h (Fig. 4E), implying the penetration of the electrolyte film by Li dendrites and short circuit of the cell [33,93]. However, we cannot observe such potential drop in the ANF-containing cells even after 1000 h (Fig. 4F and Fig. S6E-F), indicating that the ANF nanofillers greatly reinforced the PEO-LiTFSI matrices and made the CPEs mechanically stronger. Moreover, the ANF-based cells displayed lower over-potentials than the ANF-free cells, furtherly proving the lower resistances of the ANF-based CPE films. Impressively the 5% ANF-based cells nearly kept the same over-potential of around 0.10 V during the cycling.

EIS technology was utilized to disclose the impedance change of the Li/SPE/Li cells during the Li plating/stripping processes (Fig. 4G–I and Fig. S7). The semicircles at high and low frequencies were attributed to the ohmic resistance from the electrolytes ($R_e$) and the interfacial resistance between the electrolyte films and Li metals ($R_i$), respectively [5,42,93]. The 5 wt% ANF-based cells exhibited lower total resistance of 212 and 200 Ω than the pristine and 1 wt% ANF/PEO-LiTFSI electrolyte-based cells after the charge-discharge cycling at 0.025–0.50 mA $cm^{-2}$ for 200 h (4360 and 4780 Ω) and at 0.10 mA $cm^{-2}$ for 500 h (404 and 378 Ω), respectively. These results suggested that the 5 wt% ANF nano-filling in the electrolyte can greatly reduce the interface resistance between the Li metal electrodes and the CPE film and mechanically reinforce the PEO-LiTFSI matrices, in accordance with the LSV, mechanical tensile and thermostability experiments (Fig. 3). In addition, the 1 and 5 wt% ANF-based cells exhibited decreasing $R_i$ values from 644 to 272 Ω, to 278 and 69 Ω, and then to 266 and 62 Ω after the cycling at 0.025–0.50 mA $cm^{-2}$ for 200 h and then at 0.10 mA $cm^{-2}$ for 500 h, respectively, furtherly verifying the improved interfacial contact between the Li metal electrodes and the electrolyte films and also explaining the over-potential decrease phenomena during the cycling (Fig. 4D and S6C-D) [5,42,93].

The SPE films after the continuous galvanostatic cycling were also examined by SEM. We can see that a lot of Li dendrites generated on the pristine PEO-LiTFSI electrolyte surface, and some micro-cracks also formed (Figs. S8A–C), which should result in the short circuit of the cells (Fig. 4E). On the contrary, less Li dendrites formed on the 1 wt% ANF/PEO-LiTFSI electrolyte surface after the cycling (Figs. S8D–F). However, no Li dendrite was observed on the CPE film surfaces when the ANF content exceeded 3 wt% (Fig. S8G-L), and the CPE films also remained their original structure/morphology even at the cross sections (Figs. S9A–H), which furtherly proved the superior resistance against Li dendrite growth by the ANF-reinforced CPE films. These results were consistent with the aforesaid discussion that higher $Li^+$ ion transfer number ($t_{Li}^+$) and mechanical strength can delay the nucleation of Li

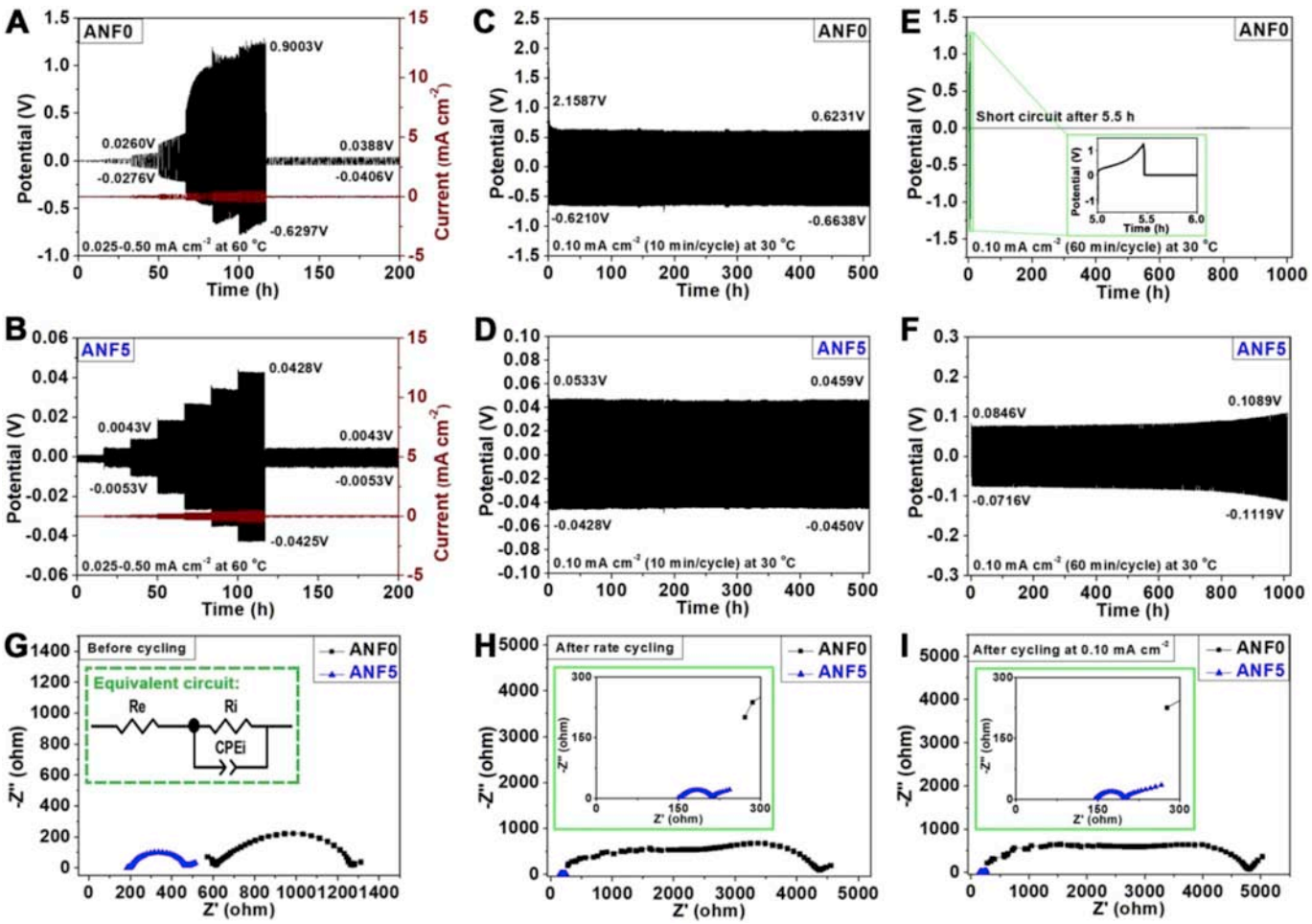


**Fig. 4.** Galvanostatic cycling curves of the (A) pristine PEO-LiTFSI and (B) 5 wt% ANF/PEO-LiTFSI electrolyte-based Li/SPE/Li cells under various current densities of 0.025–0.50 mA $cm^{-2}$ for 200 h at 60 °C. Galvanostatic cycling curves of the (C) pristine PEO-LiTFSI and (D) 5 wt% ANF/PEO-LiTFSI electrolyte-based Li/SPE/Li cells under 0.10 mA $cm^{-2}$ with the charge-discharge time of 10 min per cycle for 500 h at 30 °C. Galvanostatic cycling curves of the (E) pristine PEO-LiTFSI and (F) 5 wt% ANF/PEO-LiTFSI electrolyte-based Li/SPE/Li cells under 0.10 mA $cm^{-2}$ with the charge-discharge time of 60 min per cycle for 1000 h at 30 °C. EIS spectra of the Li/SPE/Li cells at 30 °C (G) before and after the cycling under (H) 0.025–0.50 mA $cm^{-2}$ for 200 h and (I) 0.10 mA $cm^{-2}$ (10 min per cycle) for 500 h (The insets were the equivalent circuit model and enlarged EIS spectra in high frequencies).

dendrites and inhibit the growth of Li dendrites in the electrolytes [94,95]. On one hand, the dendrite formation time (or Sand's time) follows the classic equation (3): $\tau = \pi D(C_o e/2Jt_a)^2$, where $\tau$, $C_o$, $D$, $J$, and $t_a$ represent the Sand's time, initial ion concentration, diffusion constant, current density, and anion transfer number, respectively [96,97]. The ANF-modified electrolytes showed much higher $Li^+$ cation transfer number than the pristine PEO-LiTFSI electrolyte (Table S1), which can reduce the concentration polarization, ameliorate the space charge near the electrode/electrolyte interfaces and postpone the dendrite growth, leading to less metal dendrite formation [82,94,95,98]. On the other hand, the ANF-containing CPEs had much higher mechanical strength than the pristine PEO-LiTFSI electrolyte (Fig. 3B), and thus can effectively suppress the Li dendrite growth and prevent the piercing of the CPE films from the Li dendrites [94,95,99,100]. These synergistic effects by the ANF nanofillers resulted in the greatly-enhanced interfacial resistance against Li dendrites and the long-term cycling stability of the Li/CPE/Li cells.

### 2.5. All-solid-state battery performance

As discussed above, the overall electrolyte properties including ion conductance, mechanical properties and interfacial stability against Li dendrites were greatly improved by the multifunctional ANF nanofillers. The electrolyte films were then assembled in $LiFePO_4$/CPE/Li-structured coin cells to detect their electrochemical cycling performance. When charged/discharged at 0.1 C, the solid-state LIBs exhibited increasing capacity with the operation temperature because of the increasing ionic conductivity (Fig. 5A). The 5 wt% ANF/PEO-LiTFSI electrolyte-based cells showed higher capacities of 143, 152 and 152 mAh $g^{-1}$ than the pristine electrolyte-based cells (120, 128 and 132 mAh $g^{-1}$) at 30, 40 and 50 °C, respectively. When cycled at 40 °C, all the solid-state $LiFePO_4$/Li cells showed decreasing capacities with the increase of the charge-discharge rate, and the ANF-containing cells had higher capacities than the ANF-free cells (Fig. 5B–C and Fig. S10). Among the cells, the 5 wt% ANF-based cells showed the highest capacity of 156, 160, 149 and 99 mAh $g^{-1}$ at 0.1, 0.2, 0.3 and 0.5 C, respectively, and the capacity remained 158 mAh $g^{-1}$ after the current density returned to 0.1 C again. A few researchers also reported the increasing capacity with the current density increase in initial cycling processes [101–103], which was ascribed to the improvement in the electrolyte/electrode interface contact and the cathode activation [92,101,102,104,105]. Optimizing the battery preparation process (e.g., soft polymer electrolytes as binders [106], and high-temperature treatment of the batteries before cycling [92]) can effectively enhance the interface contact for better battery performance.

When cycled at 0.2 C and 40 °C, the 5 wt% ANF-based $LiFePO_4$/Li cells exhibited higher capacity of 150 mAh $g^{-1}$ and capacity retention of 95% than the 0, 1 and 3 wt% ANF-based cells after 100 cycles (113, 122

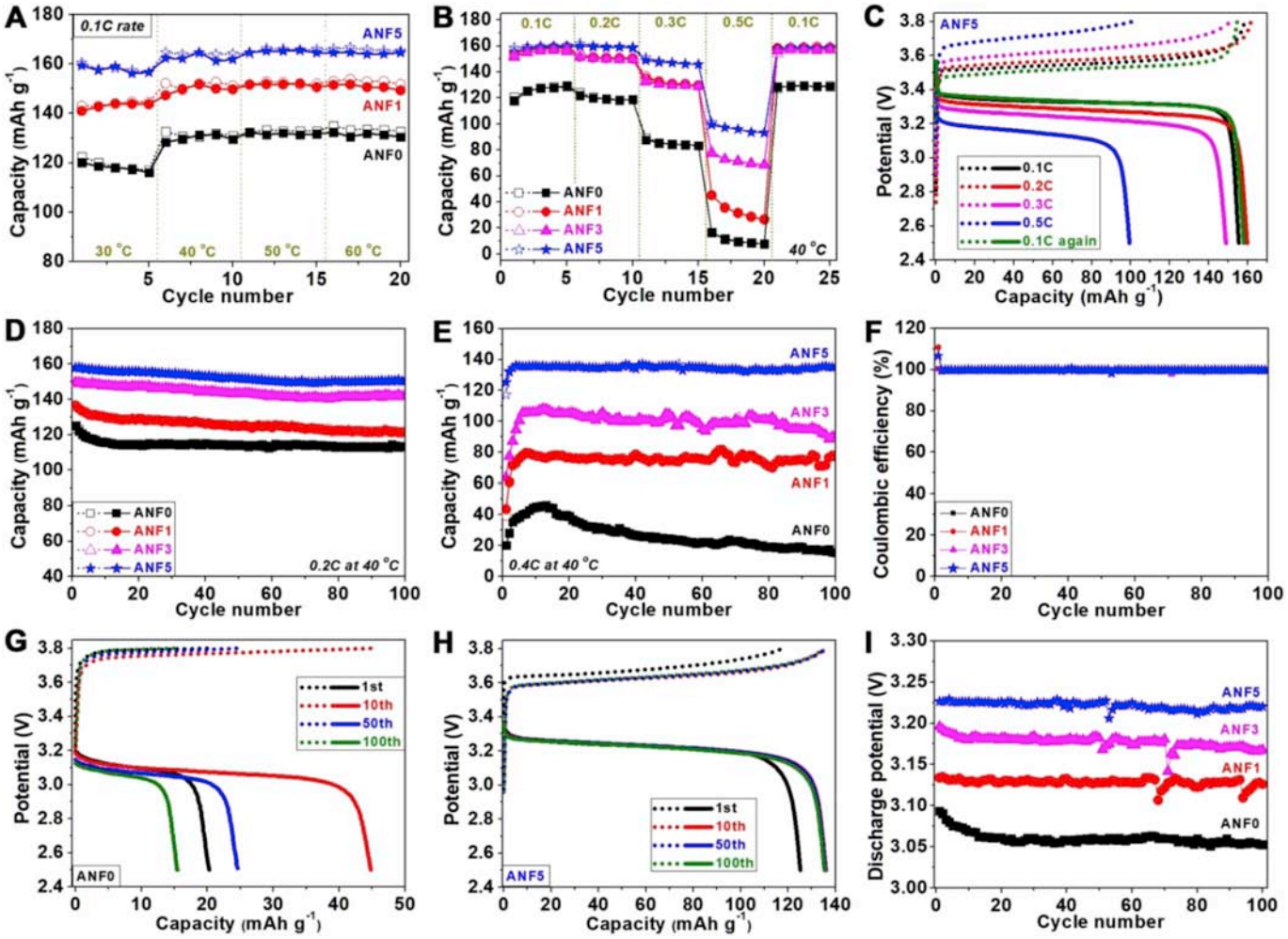


**Fig. 5.** (A) Cycling performance of the ANF/PEO-LiTFSI electrolyte-based solid-state $LiFePO_4$/Li cells at 0.1 C under various operation temperatures. (B) Rate performance of the solid-state $LiFePO_4$/Li cells at 40 °C. (C) Typical charge-discharge profiles of the solid-state cells using the 5 wt% ANF/PEO-LiTFSI electrolyte at 40 °C and various current densities. Cycling performance of the solid-state cells at (D) 0.2 C and (E) 0.4 C for 100 cycles under 40 °C, respectively. (F) Coulombic efficiencies of the solid-state cells at 0.4 C and 40 °C. The charge-discharge profiles of the solid-state cells using the (G) pristine PEO-LiTFSI and (H) 5 wt% ANF/PEO-LiTFSI electrolytes at 0.4 C and 40 °C, respectively. (I) The average discharge voltage of the solid-state cells during the 100 cycles at 0.4 C and 40 °C.

and 142 mAh $g^{-1}$), respectively (Fig. 5D). When cycled at a high rate of 0.4 C, the capacity of all the cells increased in the first 5–12 cycles (Fig. 5E), which should be ascribed to the penetration of the electrolytes into the cathodes and activation of $LiFePO_4$ [42]. The 5 wt% ANF-based cells also exhibited higher capacity of 135 mAh $g^{-1}$ than the 0, 1 and 3 wt% ANF-based cells after 100 cycles (16, 77 and 91 mAh $g^{-1}$). Moreover, all the solid-state cells had Coulombic efficiencies of nearly 100% except the first cycle (Fig. 5F), which was much higher than the traditional LIBs with the liquid electrolytes. We can also see that the ANF-based cells had less polarization than the ANF-free cells during the long-term high-rate cycling (Fig. 5G–H and Fig. S11), and the 5 wt% ANF-based cells displayed higher average discharge potential of 3.22 V than the 0, 1 and 3 wt% ANF-based cells after the 100 cycles (3.05, 3.13 and 3.17 V) (Fig. 5I). In comparison with the solid-state cells using the conventional inorganic nanofiller-modified CPEs, the multifunctional ANF-based cells exhibited superior cycling performance at relatively-low temperatures due to the combined property advantages regarding the ionic conductivity, mechanical/thermal stabilities and resistance against Li dendrites (Table S2).

EIS technology was further used to investigate the impedance change of the solid-state $LiFePO_4$/Li cells before and after the long-term cycling (Fig. S12). In the typical equivalent circuit model, $R_{ct}$, $R_i$ and $R_e$ were the charge transfer resistance, interfacial resistance and bulk resistance of the electrolytes, respectively [42,107]. The 5 wt% ANF-based cells still exhibited lower total resistances of 837 and 897 Ω than the 0, 1 and 3 wt % ANF-based cells before and after the 100 cycles (1490 and 2060 Ω, 1400 and 1760 Ω, and 895 and 1040 Ω), respectively, reflecting the much rapid charge transport in the 5 wt% ANF-based solid-state LIBs and again confirming the positive role of the ANF nanofillers [42,80].

## 3. Conclusions

In summary, multifunctional ANFs with abundant amide groups, large aspect ratio and high mechanical strength were employed to prepare ANF/PEO-LiTFSI CPE films with 3D ANF network frames by solution casting. The strong hydrogen-bond interactions between the amide groups in the 1D ANF nanofillers and the PEO chains and $TFSI^-$ anions greatly inhibited the aggregation of the ANFs in the CPEs, suppressed the crystallization of the PEO matrices, and promoted the dissociation of LiTFSI. The CPE films with 5 wt% ANFs showed much higher conductivities of $8.8 \times 10^{-5}$ and $1.0 \times 10^{-3}$ S $cm^{-1}$ at 30 and 60 °C respectively, owing to the synergistic effects of the ANF nanofillers on the PEO matrices and Li salts, and the continuous $Li^+$ ion conduction pathways at the 3D ANF framework/PEO-LiTFSI interfaces. The CPEs also displayed greatly-enhanced electrochemical, mechanical and thermal stabilities, due to the high-strength ANF nanofillers and the formed 3D frameworks.

Moreover, the CPEs exhibited higher resistance against Li dendrites (1000 h at 0.10 mA $cm^{-2}$ and 30 °C). Consequently, the ANF-based solid-state $LiFePO_4$/Li cells had superior rate performance and cycling stability (e.g., 159 mAh $g^{-1}$ at 0.1 C and 30 °C, and 135 mAh $g^{-1}$ after 100 cycles at 0.4 C and 40 °C). This work demonstration of applying multifunctional ANFs instead of the conventional inorganic nanofillers and disclosing the ion conduction mechanism offers a novel and effective CPE design way to comprehensively improve polymer electrolytes for their promising applications in high-energy and safe LIBs.

## 4. Experimental section

### 4.1. Preparation of polymer electrolytes

High-dispersity ANF solution was prepared by modifying our early method [57–59]. Specifically, 2.00 g dessicated bulk Kevlar 69, 0.40 g KOH and 200.00 g anhydrous DMSO were put in a glass bottle with a cap, and vigorously stirred for four weeks at room temperature until the formation of a dark red and viscous ANF dispersion. Pure ANF/DMSO dispersion was obtained by the following centrifugation at 10,000 rpm for at least three times (10 min per time), and dialysis for 4–12 h in fresh DMSO using a dialysis membrane to remove the excessive KOH. To fabricate ANF/PEO-LiTFSI CPE films with different ANF weight ratio, the pure ANF/DMSO solution with various amounts was added in 36 mL DMF, and stirred for 1 h to obtain high-dispersity ANF/DMSO/DMF solution. After that 1.83 g PEO (molecular weight: 60,000) was put in the ANF mixture solution, and then stirred for 12 h at 40 °C until the complete dissolution of PEO. 0.66 g bis(trifluoromethylsulphonyl)imide (LiTFSI) was first dissolved in 5 mL DMF by vigorous stirring, dropped in the ANF/PEO mixture solution, and stirred for another 12 h to prepare high-dispersity ANF/PEO/LiTFSI solution. Then the mixture solution was dropped in a Teflon plate, and dessicated at 30 °C for 12 h, 40 °C for 12 h, 50 °C for 12 h and 60 °C for 24 h to obtain the ANF/PEO-LiTFSI CPE films. The electrolyte films were put in an argon-filled glove box for at least 3 days before characterizations.

### 4.2. Materials characterizations

A Bruker D8 Focus X-ray diffraction analyzer (Cu $K_\alpha$ radiation, $\lambda$ = 0.154 nm) was used to detect the crystal structure of the electrolyte films. The morphology of the electrolytes was characterized using FEI Quanta 200F and Hitachi SU8010 SEM coupled with an energy dispersive X-ray spectroscopy (EDS). The voltages for taking SEM and EDS images were 3.0 and 20.0 kV, respectively. A FEI F20 TEM was utilized to examine the microstructures of the ANFs and electrolytes using their diluted solutions. The FT-IR spectra were obtained by a PerkinElmer Frontier FT-IR analyzer. Stress-strain curves were recorded using a GOTECH AI-7000-ST mechanical tester at a speed of 2 mm $min^{-1}$. A D840TA Q500 thermo-gravimetric analyzer was utilized to investigate the thermal stability of the electrolytes under Ar flow with a heating speed of 10 °C $min^{-1}$.

### 4.3. Electrochemical measurements

Stainless steel (SS)/SPE/SS, Li/SPE/SS, Li/SPE/Li and $LiFePO_4$/SPE/Li cells were fabricated in an Ar-filled glove box. $LiFePO_4$ electrodes with ~2.0 mg $cm^{-2}$ mass loading were obtained by coating mixture slurries of PVDF, carbon nanotube, carbon black and $LiFePO_4$ with a weight ratio of 1:0.03:0.97:8 on clean Al foils. EIS measurements were taken in a Zahner Zennium electrochemical workstation with a frequency range of $10^6$–$10^{-2}$ Hz. The $Li^+$ ion conductivity ($\sigma$) of the electrolytes was calculated by the equation: $\sigma = L/SR$, where $S$, $L$ and $R$ represented the surface area, thickness and resistance of the SPEs, respectively. The $Li^+$ ion transference number ($t_{Li}^+$) of the electrolytes were obtained by the combined measurements of EIS and chronoamperometry (CA) of the Li/SPE/Li cells at 80 °C. The $t_{Li}^+$ was calculated according to the following equation: $t_{Li}^+ = I^s R_b^s(\Delta V - I^o R_i^o)/I^o R_b^o(\Delta V - I^s R_i^s)$, where $I^o$ and $I^s$ represented the currents at the initial and steady states, respectively, $\Delta V$ represented the applied polarization potential of 0.01 V, $R_b^o$ and $R_b^s$ were the bulk resistances at the initial and steady states, respectively, and $R_i^o$ and $R_i^s$ were the electrolyte/Li interfacial resistances at the initial and steady states, respectively [80]. LSV measurements were taken in a CHI660E electrochemical workstation with a scanning rate of 1 mV $s^{-1}$. Galvanostatic charge-discharge cycle was conducted using a Land LANHE CT2001A multichannel battery tester within 2.5–3.8 V (vs. $Li/Li^+$) under different C rates (1 C = 170 mAh $g^{-1}$) and operation temperatures.

## Declaration of competing interest

The authors declare that they have no known competing financial interests or personal relationships that could have appeared to influence the work reported in this paper.

## Acknowledgment

This work is supported partially by Natural Science Foundation of Beijing Municipality (L172036), Joint Funds of the Equipment Pre-Research and Ministry of Education (6141A020225), Par-Eu Scholars Program, Science and Technology Beijing 100 Leading Talent Training Project, China Postdoctoral Science Foundation (2018M631419), the Fundamental Research Funds for the Central Universities (2017ZZD02, 2019QN001), and the NCEPU "Double First-Class" Graduate Talent Cultivation Program.

## Appendix A. Supplementary data

Supplementary data to this article can be found online at https://doi.org/10.1016/j.nanoen.2019.104398.

## References

[1] X. Zhang, X. Cheng, Q. Zhang, Nanostructured energy materials for electrochemical energy conversion and storage: a review, J. Energy Chem. 25 (2016) 967–984.
[2] Z. Gao, H. Sun, L. Fu, F. Ye, Y. Zhang, W. Luo, Y. Huang, Promises, challenges, and recent progress of inorganic solid-state electrolytes for all-solid-state lithium batteries, Adv. Mater. 30 (2018) 1–27.
[3] H. Zhang, C. Li, M. Piszcz, E. Coya, T. Rojo, L.M. Rodriguez-Martinez, M. Armand, Z. Zhou, Single lithium-ion conducting solid polymer electrolytes: advances and perspectives, Chem. Soc. Rev. 46 (2017) 797–815.
[4] L. Chen, W. Li, L.-Z. Fan, C.-W. Nan, Q. Zhang, Intercalated electrolyte with high transference number for dendrite-free solid-state lithium batteries, Adv. Funct. Mater. 29 (2019) 1901047.
[5] K. Fu, Y. Gong, J. Dai, A. Gong, X. Han, Y. Yao, C. Wang, Y. Wang, Y. Chen, C. Yan, Y. Li, E.D. Wachsman, L. Hu, Flexible, solid-state, ion-conducting membrane with 3D garnet nanofiber networks for lithium batteries, P. Natl. Acad. Sci. USA 113 (2016) 7094–7099.
[6] P. Zhu, C. Yan, M. Dirican, J. Zhu, J. Zang, R.K. Selvan, C.-C. Chung, H. Jia, Y. Li, Y. Kiyak, N. Wu, X. Zhang, $Li_{0.33}La_{0.557}TiO_3$ ceramic nanofiber-enhanced polyethylene oxide-based composite polymer electrolytes for all-solid-state lithium batteries, J. Mater. Chem. A 6 (2018) 4279–4285.
[7] X. Yao, B. Huang, J. Yin, G. Peng, Z. Huang, C. Gao, D. Liu, X. Xu, All-solid-state lithium batteries with inorganic solid electrolytes: review of fundamental science, Chin. Phys. B 25 (2016), 018802.
[8] Q. Ma, H. Zhang, C. Zhou, L. Zheng, P. Cheng, J. Nie, W. Feng, Y.S. Hu, H. Li, X. Huang, L. Chen, M. Armand, Z. Zhou, Single lithium-ion conducting polymer electrolytes based on a super-delocalized polyanion, Angew. Chem. Int. Ed. 55 (2016) 2521–2525.
[9] R. Chen, W. Qu, X. Guo, L. Li, F. Wu, The pursuit of solid-state electrolytes for lithium batteries: from comprehensive insight to emerging horizons, Mater. Horiz. 3 (2016) 487–516.
[10] L. Chen, Y. Li, S.P. Li, L.Z. Fan, C.W. Nan, J.B. Goodenough, PEO/garnet composite electrolytes for solid-state lithium batteries: from "ceramic-in-polymer" to "polymer-in-ceramic", Nano Energy 46 (2018) 176–184.
[11] D. Safanama, S. Adams, Flexible light-weight lithium-ion-conducting inorganic–organic composite electrolyte membrane, ACS Energy Lett 2 (2017) 1130–1136.
[12] S.-J. Tan, X.-X. Zeng, Q. Ma, X.-W. Wu, Y.-G. Guo, Recent advancements in polymer-based composite electrolytes for rechargeable lithium batteries, Electrochem. Energy Rev. 1 (2018) 113–138.

[13] C. Tao, M.H. Gao, B.H. Yin, B. Li, Y.P. Huang, G.W. Xu, J.J. Bao, A promising TPU/PEO blend polymer electrolyte for all-solid-state lithium ion batteries, Electrochim. Acta 257 (2017) 31–39.

[14] S. Gomari, M. Esfandeh, I. Ghasemi, All-solid-state flexible nanocomposite polymer electrolytes based on poly(ethylene oxide): lithium perchlorate using functionalized graphene, Solid State Ion. 303 (2017) 37–46.

[15] S. Suriyakumar, S. Gopi, M. Kathiresan, S. Bose, E.B. Gowd, J.R. Nair, N. Angulakshmi, G. Meligrana, F. Bella, C. Gerbaldi, A.M. Stephan, Metal organic framework laden poly(ethylene oxide) based composite electrolytes for all-solid-state Li-S and Li-metal polymer batteries, Electrochim. Acta 285 (2018) 355–364.

[16] S. Xin, Y. You, S. Wang, H.C. Gao, Y.X. Yin, Y.G. Guo, Solid-state lithium metal batteries promoted by nanotechnology: progress and prospects, ACS Energy Lett 2 (2017) 1385–1394.

[17] L. Long, S. Wang, M. Xiao, Y. Meng, Polymer electrolytes for lithium polymer batteries, J. Mater. Chem. A 4 (2016) 10038–10039.

[18] Z.P. Wan, D.N. Lei, W. Yang, C. Liu, K. Shi, X.G. Hao, L. Shen, W. Lv, B.H. Li, Q. H. Yang, F.Y. Kang, Y.B. He, Low resistance-integrated all-solid-state battery achieved by $Li_7La_3Zr_2O_{12}$ nanowire upgrading polyethylene oxide (PEO) composite electrolyte and PEO cathode binder, Adv. Funct. Mater. 29 (2019) 1805301.

[19] X.F. Yang, Q. Sun, C.T. Zhao, X.J. Gao, K.R. Adair, Y.L. Liu, J. Luo, X.T. Lin, J. N. Liang, H. Huang, L. Zhang, R. Yang, S.G. Lu, R.Y. Li, X.L. Sun, High-areal-capacity all-solid-state lithium batteries enabled by rational design of fast ion transport channels in vertically-aligned composite polymer electrodes, Nano Energy 61 (2019) 567–575.

[20] J. Zhang, N. Zhao, M. Zhang, P.K. Chu, X. Guo, Z. Di, X. Wang, H. Li, Flexible and ion-conducting membrane electrolytes for solid-state lithium batteries: dispersion of garnet nanoparticles in insulating polyethylene oxide, Nano Energy 28 (2016) 447–454.

[21] X.F. Yuan, C. Sun, J.N. Duan, J.M. Fan, R.M. Yuan, J.J. Chen, J.K. Chang, M. S. Zheng, Q.F. Dong, A polyoxometalate-based polymer electrolyte with an improved electrode interface and ion conductivity for high-safety all-solid-state batteries, J. Mater. Chem. A 7 (2019) 15924–15932.

[22] X. Li, D. Wang, H. Wang, H. Yan, Z. Gong, Y. Yang, Poly(ethylene oxide)–$Li_{10}SnP_2S_{12}$ composite polymer electrolyte enables high-performance all-solid-state lithium sulfur battery, ACS Appl. Mater. Interfaces 11 (2019) 22745–22753.

[23] J. Hu, W.H. Wang, B.H. Zhou, Y.Z. Feng, X.L. Xie, Z.G. Xue, Poly(ethylene oxide)-based composite polymer electrolytes embedding with ionic bond modified nanoparticles for all-solid-state lithium-ion battery, J. Membr. Sci. 575 (2019) 200–208.

[24] Y. Sun, X.W. Zhan, J.Z. Hu, Y.K. Wang, S. Gao, Y.H. Shen, Y.T. Cheng, Improving ionic conductivity with bimodal-sized $Li_7La_3Zr_2O_{12}$ fillers for composite polymer electrolytes, ACS Appl. Mater. Interfaces 11 (2019) 12467–12475.

[25] C.-Z. Zhao, X.-Q. Zhang, X.-B. Cheng, R. Zhang, R. Xu, P.-Y. Chen, H.-J. Peng, J.-Q. Huang, Q. Zhang, An anion-immobilized composite electrolyte for dendrite-free lithium metal anodes, P. Natl. Acad. Sci. USA 114 (2017) 11069.

[26] Z. He, L. Chen, B. Zhang, Y. Liu, L.-Z. Fan, Flexible poly(ethylene carbonate)/garnet composite solid electrolyte reinforced by poly(vinylidene fluoride-hexafluoropropylene) for lithium metal batteries, J. Power Sources 392 (2018) 232–238.

[27] W. Liu, N. Liu, J. Sun, P.C. Hsu, Y. Li, H.W. Lee, Y. Cui, Ionic conductivity enhancement of polymer electrolytes with ceramic nanowire fillers, Nano Lett. 15 (2015) 2740–2745.

[28] J. Zhang, X. Zang, H. Wen, T. Dong, J. Chai, Y. Li, B. Chen, J. Zhao, S. Dong, J. Ma, L. Yue, Z. Liu, X. Guo, G. Cui, L. Chen, High-voltage and free-standing poly(propylene carbonate)/$Li_{6.75}La_3Zr_{1.75}Ta_{0.25}O_{12}$ composite solid electrolyte for wide temperature range and flexible solid lithium ion battery, J. Mater. Chem. A 5 (2017) 4940–4948.

[29] H. Xu, P.-H. Chien, J. Shi, Y. Li, N. Wu, Y. Liu, Y.-Y. Hu, J.B. Goodenough, High-performance all-solid-state batteries enabled by salt bonding to perovskite in poly(ethylene oxide), P. Natl. Acad. Sci. USA 116 (2019) 18815.

[30] Z.J. Sun, Y.H. Li, S.Y. Zhang, L. Shi, H. Wu, H.T. Bu, S.J. Ding, g-$C_3N_4$ nanosheets enhanced solid polymer electrolytes with excellent electrochemical performance, mechanical properties, and thermal stability, J. Mater. Chem. A 7 (2019) 11069–11076.

[31] W. Liu, D. Lin, J. Sun, G. Zhou, Y. Cui, Improved lithium ionic conductivity in composite polymer electrolytes with oxide-ion conducting nanowires, ACS Nano 10 (2016) 11407–11413.

[32] W. Liu, S.W. Lee, D. Lin, F. Shi, S. Wang, A.D. Sendek, Y. Cui, Enhancing ionic conductivity in composite polymer electrolytes with well-aligned ceramic nanowires, Nat. Energy 2 (2017) 1–7.

[33] T. Yang, J. Zheng, Q. Cheng, Y.-Y. Hu, C.K. Chan, Composite polymer electrolytes with $Li_7La_3Zr_2O_{12}$ garnet-type nanowires as ceramic fillers: mechanism of conductivity enhancement and role of doping and morphology, ACS Appl. Mater. Interfaces 9 (2017) 21773–21780.

[34] J. Zheng, P. Wang, H. Liu, Y.-Y. Hu, Interface-enabled ion conduction in $Li_{10}GeP_2S_{12}$–poly(ethylene oxide) hybrid electrolytes, ACS Appl. Energy Mater. 2 (2019) 1452–1459.

[35] W. Tang, S. Tang, C. Zhang, Q. Ma, Q. Xiang, Y.-W. Yang, J. Luo, Simultaneously enhancing the thermal stability, mechanical modulus, and electrochemical performance of solid polymer electrolytes by incorporating 2D sheets, Adv. Energy Mater. 8 (2018) 1800866.

[36] K.Q. He, C.L. Chen, R. Fan, C. Liu, C.Z. Liao, Y. Xu, J.N. Tang, R.K.Y. Li, Polyethylene oxide/garnet-type $Li_{6.4}La_3Zr_{1.4}Nb_{0.6}O_{12}$ composite electrolytes with improved electrochemical performance for solid state lithium rechargeable batteries, Compos. Sci. Technol. 175 (2019) 28–34.

[37] X. Fu, C. Li, Y. Wang, L.P. Kovatch, L. Scudiero, J. Liu, W. Zhong, Building ion-conduction highways in polymeric electrolytes by manipulating protein configuration, ACS Appl. Mater. Interfaces 10 (2018) 4726–4736.

[38] W. Li, S. Zhang, B. Wang, S. Gu, D. Xu, J. Wang, C. Chen, Z. Wen, Nanoporous adsorption effect on alteration of the $Li^+$ diffusion pathway by a highly ordered porous electrolyte additive for high-rate all-solid-state lithium metal batteries, ACS Appl. Mater. Interfaces 10 (2018) 23874–23882.

[39] P.Q. Lin, P. Liu, H.Q. Lin, Z.Y. Dai, Z.B. Zhang, D.J. Chen, Ionic conductivity promotion of polymer membranes with oxygen-ion conducting nanowires for rechargeable lithium batteries, J. Membr. Sci. 580 (2019) 92–100.

[40] D. Lin, W. Liu, Y. Liu, H.R. Lee, P.C. Hsu, K. Liu, Y. Cui, High ionic conductivity of composite solid polymer electrolyte via in situ synthesis of monodispersed $SiO_2$ nanospheres in poly(ethylene oxide), Nano Lett. 16 (2016) 459–465.

[41] M. Dirican, C.Y. Yan, P. Zhu, X.W. Zhang, Composite solid electrolytes for all-solid-state lithium batteries, Mater. Sci. Eng. R. 136 (2019) 27–46.

[42] L. Liu, L. Chu, B. Jiang, M. Li, $Li_{1.4}Al_{0.4}Ti_{1.6}(PO_4)_3$ nanoparticle-reinforced solid polymer electrolytes for all-solid-state lithium batteries, Solid State Ion. 331 (2019) 89–95.

[43] L. Zhu, P. Zhu, Q. Fang, M. Jing, X. Shen, L. Yang, A novel solid PEO/LLTO-nanowires polymer composite electrolyte for solid-state lithium-ion battery, Electrochim. Acta 292 (2018) 718–726.

[44] D. Lin, P.Y. Yuen, Y. Liu, W. Liu, N. Liu, R.H. Dauskardt, Y. Cui, A silica-aerogel-reinforced composite polymer electrolyte with high ionic conductivity and high modulus, Adv. Mater. 30 (2018) 1802661.

[45] X. Wang, H. Zhai, B. Qie, Q. Cheng, A. Li, J. Borovilas, B. Xu, C. Shi, T. Jin, X. Liao, Y. Li, X. He, S. Du, Y. Fu, M. Dontigny, K. Zaghib, Y. Yang, Rechargeable solid-state lithium metal batteries with vertically aligned ceramic nanoparticle/polymer composite electrolyte, Nano Energy 60 (2019) 205–212.

[46] H. Zhai, P. Xu, M. Ning, Q. Cheng, J. Mandal, Y. Yang, A flexible solid composite electrolyte with vertically aligned and connected ion-conducting nanoparticles for lithium batteries, Nano Lett. 17 (2017) 3182–3187.

[47] J. Bae, Y. Li, J. Zhang, X. Zhou, F. Zhao, Y. Shi, J.B. Goodenough, G. Yu, A 3D nanostructured hydrogel-framework-derived high-performance composite polymer lithium-ion electrolyte, Angew. Chem. Int. Ed. 57 (2018) 2096–2100.

[48] H. Xie, C. Yang, K. Fu, Y. Yao, F. Jiang, E. Hitz, B. Liu, S. Wang, L. Hu, Flexible, scalable, and highly conductive garnet-polymer solid electrolyte templated by bacterial cellulose, Adv. Energy Mater. 8 (2018) 1703474.

[49] D. Li, L. Chen, T. Wang, L.-Z. Fan, 3D fiber-network-reinforced bicontinuous composite solid electrolyte for dendrite-free lithium metal batteries, ACS Appl. Mater. Interfaces 10 (2018) 7069–7078.

[50] Y. Lim, H.-A. Jung, H. Hwang, Fabrication of PEO-PMMA-$LiClO_4$-based solid polymer electrolytes containing silica aerogel particles for all-solid-state lithium batteries, Energies 11 (2018) 2559.

[51] X.-Y. Yu, M. Xiao, S.-J. Wang, Q.-Q. Zhao, Y.-Z. Meng, Fabrication and characterization of PEO/PPC polymer electrolyte for lithium-ion battery, J. Appl. Polym. Sci. 115 (2010) 2718–2722.

[52] A.M. Rocco, R.P. Pereira, Solid electrolytes based on poly(ethylene oxide)/poly(4-vinyl phenol-co-2-hydroxyethyl methacrylate) blends and $LiClO_4$, Solid State Ion. 279 (2015) 78–89.

[53] J. Shim, D.-G. Kim, H.J. Kim, J.H. Lee, J.-H. Baik, J.-C. Lee, Novel composite polymer electrolytes containing poly(ethylene glycol)-grafted graphene oxide for all-solid-state lithium-ion battery applications, J. Mater. Chem. A 2 (2014) 13873–13883.

[54] R.-J. Chen, Y.-B. Zhang, T. Liu, B.-Q. Xu, Y.-H. Lin, C.-W. Nan, Y. Shen, Addressing the interface issues in all-solid-state bulk-type lithium ion battery via an all-composite approach, ACS Appl. Mater. Interfaces 9 (2017) 9654–9661.

[55] C. Ma, K. Dai, H. Hou, X. Ji, L. Chen, D.G. Ivey, W. Wei, High ion-conducting solid-state composite electrolytes with carbon quantum dot nanofillers, Adv. Sci. 5 (2018) 1700996.

[56] P. Zhu, C. Yan, M. Dirican, J. Zhu, J. Zang, R.K. Selvan, C.-C. Chung, H. Jia, Y. Li, Y. Kiyak, N. Wu, X. Zhang, $Li_{0.33}La_{0.557}TiO_3$ ceramic nanofiber-enhanced polyethylene oxide-based composite polymer electrolytes for all-solid-state lithium batteries, J. Mater. Chem. 6 (2018) 4279–4285.

[57] J. Lyu, L. Liu, X. Zhao, Y. Shang, T. Zhao, T. Li, Facile fabrication of multifunctional aramid nanofiber films by spin coating, J. Mater. Eng. Perform. 25 (2016) 4757–4763.

[58] J. Lyu, M.D. Hammig, L. Liu, L. Xu, H. Chi, C. Uher, T. Li, N.A. Kotov, Stretchable conductors by kirigami patterning of aramid-silver nanocomposites with zero conductance gradient, Appl. Phys. Lett. 111 (2017), 161901-161901.

[59] J. Lyu, X. Wang, L. Liu, Y. Kim, E.K. Tanyi, H. Chi, W. Feng, L. Xu, T. Li, M. A. Noginov, C. Uher, M.D. Hammig, N.A. Kotov, High strength conductive composites with plasmonic nanoparticles aligned on aramid nanofibers, Adv. Funct. Mater. 26 (2016) 8435–8445.

[60] S.-O. Tung, S. Ho, M. Yang, R. Zhang, N.A. Kotov, A dendrite-suppressing composite ion conductor from aramid nanofibres, Nat. Commun. 6 (2015), 6152-6152.

[61] S. Hu, S. Lin, Y. Tu, J. Hu, Y. Wu, G. Liu, F. Li, F. Yu, T. Jiang, Novel aramid nanofiber-coated polypropylene separators for lithium ion batteries, J. Mater. Chem. A 4 (2016) 3513–3526.

[62] J. Lyu, X. Zhao, X. Hou, Y. Zhang, T. Li, Y. Yan, Electromagnetic interference shielding based on a high strength polyaniline-aramid nanocomposite, Compos. Sci. Technol. 149 (2017) 159–165.

[63] H. Zhang, Y. Zhang, T. Xu, A.E. John, Y. Li, W. Li, B. Zhu, Poly(m-phenylene isophthalamide) separator for improving the heat resistance and power density of lithium-ion batteries, J. Power Sources 329 (2016) 8–16.

[64] X. Zhang, N. Li, Z. Hu, J. Yu, Y. Wang, J. Zhu, Poly(p-phenylene terephthalamide) modified PE separators for lithium ion batteries, J. Membr. Sci. 581 (2019) 355–361.

[65] Q. Zhou, J. Ma, S. Dong, X. Li, G. Cui, Intermolecular chemistry in solid polymer electrolytes for high-energy-density lithium batteries, Adv. Mater. (2019) 1902029.

[66] Q. Zhang, K. Liu, F. Ding, X. Liu, Recent advances in solid polymer electrolytes for lithium batteries, Nano Res. 10 (2017) 4139–4174.

[67] K. Vignarooban, M.A.K.L. Dissanayake, I. Albinsson, B.E. Mellander, Effect of $TiO_2$ nano-filler and EC plasticizer on electrical and thermal properties of poly (ethylene oxide) (PEO) based solid polymer electrolytes, Solid State Ion. 266 (2014) 25–28.

[68] X.-B. Fu, L.-Y. Yang, J.-Q. Ma, G. Yang, Y.-F. Yao, Q. Chen, Revealing structure and dynamics in host–guest supramolecular crystalline polymer electrolytes by solid-state NMR: applications to β-CD-polyether/$Li^+$ crystal, Polymer 105 (2016) 310–317.

[69] E. Kharlampieva, V. Kozlovskaya, S.A. Sukhishvili, Layer-by-layer hydrogen-bonded polymer films: from fundamentals to applications, Adv. Mater. 21 (2009) 3053–3065.

[70] S.-O. Tung, S. Ho, M. Yang, R. Zhang, N.A. Kotov, A dendrite-suppressing composite ion conductor from aramid nanofibres, Nat. Commun. 6 (2015) 6152.

[71] L. Yao, C. Lee, J. Kim, Fabrication of electrospun meta-aramid nanofibers in different solvent systems, Fiber. Polym 11 (2010) 1032–1040.

[72] A.M. Stephan, T.P. Kumar, N. Angulakshmi, P.S. Salini, R. Sabarinathan, A. Srinivasan, S. Thomas, Influence of calix[2]-p-benzo[4]pyrrole on the electrochemical properties of poly(ethylene oxide)-based electrolytes for lithium batteries, J. Appl. Polym. Sci. 120 (2011) 2215–2221.

[73] A. Blazejczyk, W. Wieczorek, R. Kovarsky, D. Golodnitsky, E. Peled, L.G. Scanlon, G.B. Appetecchi, B. Scrosati, Novel solid polymer electrolytes with single lithium-ion transport, J. Electrochem. Soc. 151 (2004) A1762–A1766.

[74] A. Blazejczyk, M. Szczupak, W. Wieczorek, P. Cmoch, G.B. Appetecchi, B. Scrosati, R. Kovarsky, D. Golodnitsky, E. Peled, Anion-binding calixarene receptors: synthesis, microstructure, and effect on properties of polyether electrolytes, Chem. Mater. 17 (2005) 1535–1547.

[75] K. Karthik, R. Murugan, Lithium garnet based free-standing solid polymer composite membrane for rechargeable lithium battery, J. Solid State Electrochem. 22 (2018) 2989–2998.

[76] M. Sasikumar, M. Raja, R.H. Krishna, A. Jagadeesan, P. Sivakumar, S. Rajendran, Influence of hydrothermally synthesized cubic-structured $BaTiO_3$ ceramic fillers on ionic conductivity, mechanical integrity, and thermal behavior of P (VDF–HFP)/PVAc-based composite solid polymer electrolytes for lithium-ion batteries, J. Phys. Chem. C 122 (2018) 25741–25752.

[77] A.S. Pandian, X.C. Chen, J. Chen, B.S. Lokitz, R.E. Ruther, G. Yang, K. Lou, J. Nanda, F.M. Delnick, N.J. Dudney, Facile and scalable fabrication of polymer-ceramic composite electrolyte with high ceramic loadings, J. Power Sources 390 (2018) 153–164.

[78] Y. Zhao, Z. Huang, S. Chen, B. Chen, J. Yang, Q. Zhang, F. Ding, Y. Chen, X. Xu, A promising PEO/LAGP hybrid electrolyte prepared by a simple method for all-solid-state lithium batteries, Solid State Ion. 295 (2016) 65–71.

[79] K. Zhu, Y. Liu, J. Liu, A fast charging/discharging all-solid-state lithium ion battery based on PEO-MIL-53(Al)-LiTFSI thin film electrolyte, RSC Adv. 4 (2014) 42278–42284.

[80] O. Sheng, C. Jin, J. Luo, H. Yuan, H. Huang, Y. Gan, J. Zhang, Y. Xia, C. Liang, W. Zhang, X. Tao, $Mg_2B_2O_5$ nanowire enabled multifunctional solid-state electrolytes with high ionic conductivity, excellent mechanical properties, and flame-retardant performance, Nano Lett. 18 (2018) 3104–3112.

[81] L. Porcarelli, K. Manojkumar, H. Sardon, O. Llorente, A.S. Shaplov, K. Vijayakrishna, C. Gerbaldi, D. Mecerreyes, Single ion conducting polymer electrolytes based on versatile polyurethanes, Electrochim. Acta 241 (2017) 526–534.

[82] Y. Xu, Y. Zhou, T. Li, S. Jiang, X. Qian, Q. Yue, Y. Kang, Multifunctional covalent organic frameworks for high capacity and dendrite-free lithium metal batteries, Energy Storage Mater. (2019), https://doi.org/10.1016/j.ensm.2019.10.005. In press.

[83] W. Wang, E. Yi, A.J. Fici, R.M. Laine, J. Kieffer, Lithium ion conducting poly (ethylene oxide)-based solid electrolytes containing active or passive ceramic nanoparticles, J. Phys. Chem. C 121 (2017) 2563–2573.

[84] X. Zhang, J. Xie, F. Shi, D. Lin, Y. Liu, W. Liu, A. Pei, Y. Gong, H. Wang, K. Liu, Y. Xiang, Y. Cui, Vertically aligned and continuous nanoscale ceramic–polymer interfaces in composite solid polymer electrolytes for enhanced ionic conductivity, Nano Lett. 18 (2018) 3829–3838.

[85] S. Kalnaus, A.S. Sabau, W.E. Tenhaeff, N.J. Dudney, C. Daniel, Design of composite polymer electrolytes for Li ion batteries based on mechanical stability criteria, J. Power Sources 201 (2012) 280–287.

[86] M. Liu, Z. Cheng, S. Ganapathy, C. Wang, L.A. Haverkate, M. Tułodziecki, S. Unnikrishnan, M. Wagemaker, Tandem interface and bulk Li-ion transport in a hybrid solid electrolyte with microsized active filler, ACS Energy Lett 4 (2019) 2336–2342.

[87] G. Derrien, J. Hassoun, S. Sacchetti, S. Panero, Nanocomposite PEO-based polymer electrolyte using a highly porous, super acid zirconia filler, Solid State Ion. 180 (2009) 1267–1271.

[88] L. Liu, X. Wu, T. Li, Novel polymer electrolytes based on cationic polyurethane with different alkyl chain length, J. Power Sources 249 (2014) 397–404.

[89] S.R. Mustapa, M.M. Aung, A. Ahmad, A. Mansor, L. TianKhoon, Preparation and characterization of Jatropha oil-based Polyurethane as non-aqueous solid polymer electrolyte for electrochemical devices, Electrochim. Acta 222 (2016) 293–302.

[90] F. Croce, G.B. Appetecchi, L. Persi, B. Scrosati, Nanocomposite polymer electrolytes for lithium batteries, Nature 394 (1998) 456–458.

[91] Z. Wang, X. Huang, L. Chen, Understanding of effects of nano-$Al_2O_3$ particles on ionic conductivity of composite polymer electrolytes, Electrochem. Solid State Lett. 6 (2003) E40–E44.

[92] S.H.-S. Cheng, K.-Q. He, Y. Liu, J.-W. Zha, M. Kamruzzaman, R.L.-W. Ma, Z.-M. Dang, R.K.Y. Li, C.Y. Chung, Electrochemical performance of all-solid-state lithium batteries using inorganic lithium garnets particulate reinforced PEO/$LiClO_4$ electrolyte, Electrochim. Acta 253 (2017) 430–438.

[93] X. Ke, Y. Cheng, J. Liu, L. Liu, N. Wang, J. Liu, C. Zhi, Z. Shi, Z. Guo, Hierarchically bicontinuous porous copper as advanced 3D skeleton for stable lithium storage, ACS Appl. Mater. Interfaces 10 (2018) 13552–13561.

[94] G.M. Stone, S.A. Mullin, A.A. Teran, D.T. Hallinan, A.M. Minor, A. Hexemer, N. P. Balsara, Resolution of the modulus versus adhesion dilemma in solid polymer electrolytes for rechargeable lithium metal batteries, J. Electrochem. Soc. 159 (2012) A222–A227.

[95] J. Bao, G. Shi, C. Tao, C. Wang, C. Zhu, L. Cheng, G. Qian, C. Chen, Polycarbonate-based polyurethane as a polymer electrolyte matrix for all-solid-state lithium batteries, J. Power Sources 389 (2018) 84–92.

[96] C. Brissot, M. Rosso, J.N. Chazalviel, S. Lascaud, Dendritic growth mechanisms in lithium/polymer cells, J. Power Sources 81–82 (1999) 925–929.

[97] M. Rosso, C. Brissot, A. Teyssot, M. Dollé, L. Sannier, J.-M. Tarascon, R. Bouchet, S. Lascaud, Dendrite short-circuit and fuse effect on Li/polymer/Li cells, Electrochim. Acta 51 (2006) 5334–5340.

[98] J.N. Chazalviel, Electrochemical aspects of the generation of ramified metallic electrodeposits, Phys. Rev. A 42 (1990) 7355–7367.

[99] H. Zhai, P. Xu, M. Ning, Q. Cheng, J. Mandal, Y. Yang, A flexible solid composite electrolyte with vertically aligned and connected ion-conducting nanoparticles for lithium batteries, Nano Lett. 17 (2017) 3182–3187.

[100] R. Khurana, J.L. Schaefer, L.A. Archer, G.W. Coates, Suppression of lithium dendrite growth using cross-linked polyethylene/poly(ethylene oxide) electrolytes: a new approach for practical lithium-metal polymer batteries, J. Am. Chem. Soc. 136 (2014) 7395–7402.

[101] Y. Zhao, Y. Bai, Y. Bai, M. An, G. Chen, W. Li, C. Li, Y. Zhou, A rational design of solid polymer electrolyte with high salt concentration for lithium battery, J. Power Sources 407 (2018) 23–30.

[102] R. Liu, P. He, Z. Wu, F. Guo, B. Huang, Q. Wang, Z. Huang, C.-a. Wang, Y. Li, PEO/hollow mesoporous polymer spheres composites as electrolyte for all solid state lithium ion battery, J. Electroanal. Chem. 822 (2018) 105–111.

[103] B. Zhang, Y. Zhang, N. Zhang, J. Liu, L. Cong, J. Liu, L. Sun, A. Mauger, C. M. Julien, H. Xie, X. Pan, Synthesis and interface stability of polystyrene-poly (ethylene glycol)-polystyrene triblock copolymer as solid-state electrolyte for lithium-metal batteries, J. Power Sources 428 (2019) 93–104.

[104] Y.-C. Jung, S.-M. Lee, J.-H. Choi, S.S. Jang, D.-W. Kim, All solid-state lithium batteries assembled with hybrid solid electrolytes, J. Electrochem. Soc. 162 (2015) A704–A710.

[105] B. Chen, Z. Huang, X. Chen, Y. Zhao, Q. Xu, P. Long, S. Chen, X. Xu, A new composite solid electrolyte PEO/$Li_{10}GeP_2S_{12}$/SN for all-solid-state lithium battery, Electrochim. Acta 210 (2016) 905–914.

[106] Z. Zhang, Y. Zhao, S. Chen, D. Xie, X. Yao, P. Cui, X. Xu, An advanced construction strategy of all-solid-state lithium batteries with excellent interfacial compatibility and ultralong cycle life, J. Mater. Chem. A 5 (2017) 16984–16993.

[107] W. Zhang, J. Nie, F. Li, Z.L. Wang, C. Sun, A durable and safe solid-state lithium battery with a hybrid electrolyte membrane, Nano Energy 45 (2018) 413–419.